Journal of Fluids Engineering – ASME

Radial pressure wave behavior in transient laminar pipe flows under different flow perturbations

Tong-Chuan Che
Department of Civil and Environmental Engineering, The Hong Kong Polytechnic University
Hong Kong SAR, China
tong-chuan.che@connect.polyu.hk

Huan-Feng Duan[1]
Department of Civil and Environmental Engineering, The Hong Kong Polytechnic University
Hong Kong SAR, China
hf.duan@polyu.edu.hk

Pedro J. Lee
Department of Civil and Natural Resources Engineering, The University of Canterbury
Private Bag 4800, Christchurch, New Zealand
pedro.lee@canterbury.ac.nz

Silvia Meniconi
Department of Civil and Environmental Engineering, University of Perugia
06125 Perugia, Italy
silvia.meniconi@unipg.it

Bin Pan
Department of Civil and Environmental Engineering, The Hong Kong Polytechnic University
Hong Kong SAR, China
bin.pan@connect.polyu.hk

Bruno Brunone
Department of Civil and Environmental Engineering, University of Perugia
06125 Perugia, Italy
bruno.brunone@unipg.it

[1] Corresponding author.

The following publication Che, T. C., Duan, H. F., Lee, P. J., Meniconi, S., Pan, B., & Brunone, B. (2018). Radial pressure wave behavior in transient laminar pipe flows under different flow perturbations. Journal of Fluids Engineering, 140(10), 101203 is available at https://doi.org/10.1115/1.4039711.

ABSTRACT

The study of transient pressure waves in both low and high frequency domains has been a new research area to provide potentially high-resolution pipe fault detection methods. In previous research works, radial pressure waves were evidently observed after stopping the laminar pipe flows by valve closures, but the generation mechanism and components of these radial pressure waves are unclear. This paper intends to clarify this phenomenon. To this end, this study firstly addresses the inefficiencies of the current numerical scheme for the full two-dimensional (full-2D) water hammer model. The modified efficient full-2D model is then implemented into a practical reservoir-pipeline-valve system, which is validated by the well-established analytical solutions. The generation mechanism and components of the radial pressure waves, caused by different flow perturbations from valve operations, in transient laminar flows are investigated systematically using this efficient full-2D model. The results indicate that non-uniform changes in the initial velocity profile form pressure gradients along the pipe radius. The existence of these radial pressure gradients is the driving force of the formation of radial flux and radial pressure waves. In addition, high radial modes can be excited, and the frequency of flow perturbations by valve oscillation can redistribute the energy entrapped in each high radial mode.

INTRODUCTION

Water hammer or hydraulic transients are a series of positive and negative pressure waves (i.e., unsteady pressure fluctuations), with propagation speeds up to 1 km/s in elastic water pipelines. These fluctuations are often caused by sudden changes in initial and boundary flow conditions of fluid piping systems. In urban water supply systems (UWSS), water hammer is easily and frequently triggered by opening/closing of valves, starting/stopping of pumps and variations in inflow or outflow. Understanding and predicting these pressure fluctuations are of great practical importance, because water hammer may cause major problems, such as noise and vibration, cavitation erosion, hydraulic equipment damage, and pipe collapse. The traditional application of transient analysis is mainly for the prediction of pressure history in pipeline systems to assist the design and evaluation of pipeline strength and placement of transient control devices [1-3].

For many years, one-dimensional (1D) and quasi-2D water hammer models are commonly adopted for predicting such pressure history. In these models, radial inertia and viscous terms are neglected due to the slight compressibility of the water and the small expansion of the pipe wall (referred to as the plane wave assumption) [4]. Both 1D and quasi-2D models consist of a set of partial differential equations (PDEs) and appropriate numerical schemes are used to approximate the solutions. The most popular scheme for the 1D model is the method of characteristics (MOC) for its simplicity, stability and efficiency of numerical implementation [1, 5]. For the quasi-2D model, the Vardy-Hwang scheme [6] is a commonly used scheme, (e.g. [7]), which solves

the axial direction by the MOC and the radial direction by the finite difference method (FDM). The merits of this scheme are well summarized in [5], but it has been proved to be very computationally intensive. Zhao and Ghidaoui [8] addressed the inefficiency problem of the Vary-Hwang scheme by decoupling the original scheme into two tridiagonal systems. This makes it possible to use the quasi-2D model in practical pipelines, such as reservoir-pipeline-valve (RPV) systems. Thereafter, Duan, Ghidaoui and Tung [9] extended this efficient quasi-2D model to complex pipe systems with multiple pipe connections. Many application results have demonstrated that both 1D and quasi-2D models, based on the plane wave assumption, give satisfactory results in the prediction of pressure history for the design purpose [6, 10, 11]. More recently, various commercial computational fluid dynamics (CFD) packages, considering the pressure variation along the pipe radius, have been applied successfully to investigate transient pipe flows, e.g., transient wave propagation and flow evolution [12], and transient wave-blockage interaction [13]. Similarly, the computational efficiency of these CFD packages has become the main concern for their extensive applications, especially for practical pipeline systems.

In recent years, the transient analysis is becoming more widely used in many high accuracy demanding fields. For example, pipeline defects (e.g., leakage and blockage) detection in the UWSS has attracted more attention due to the water and energy shortage worldwide. Many methods have been proposed for pipeline defects detection, among which the transient-based method [14, 15] is regarded as a promising detection approach, because it has the desirable merits of high efficiency, low cost and

non-destructive applications. The injected transient wave is modified by pipeline defects as it propagates in the pipeline. The wave contains physical information on the size and location of these defects, which can be detected inversely based on the modified transient wave. Many theoretical and experimental studies [16-28] have successfully applied this transient-based method using low-frequency waves (LFW), which mainly depends on the longitudinal and plane wave propagating features. Lee, Duan, Tuck and Ghidaoui [29] found that LFW have a long detection range, but fault detection using LFW suffers from low spatial resolution; whist high-frequency waves (HFW) have the opposite features. It is suggested that practical defects detection should involve both the LFW and HFW; where LFW is first used to identify potential defective sections, followed by the application of HFW in the region of interest to pinpoint the defects [29]. However, as the wavelength approaches the diameter of the pipe, radial pressure waves will be generated and the plane wave assumption in current 1D and quasi-2D models might be violated.

The full-2D water hammer model, including all terms neglected in current 1D and quasi-2D models, is a potential tool for investigating the radial pressure waves excited by HFW. The full-2D model was proposed by Mitra and Rouleau [30] to observe the radial and axial variations of transient pressure waves caused by valve closures. The full-2D model was solved numerically by an implicit matrix factorization method; in this way, the 2D problem was decomposed into two 1D problems, saving significant computational effort. Despite this improvement, the numerical method in [30] still contains inefficiencies due to (i) the complexity of coefficient matrixes; and (ii) the application of

uniform grids, because very fine grids were needed to capture the detailed physical phenomena in the boundary layer near the pipe wall. Recently, a high-order finite volume scheme for the full-2D model was developed [31, 32] to investigate the properties of HFW in a pressurized water pipeline. However, this previous study was limited to relatively idealized flow situations, i.e., inviscid and initially stagnant flows; thus, their results mainly provided basic understanding of acoustic wave propagation in a water-filled pipeline. Meanwhile, the way of transient generation adopted in this previous study was also very simple, and common ways of transient generation, such as valve operations in practical RPV systems, were not included and examined.

In fact, flows in the practical UWSS always have non-uniform (or non-plane) velocity profiles due to the existence of viscosity; and in general, transients are generated by a change in flowrate due to hydraulic device operations (e.g., valves and pumps). Such practical flow situations might have an influence on the generation and propagation of radial pressure waves. For example, radial pressure waves were observed by Mitra and Rouleau [30] after stopping a laminar flow by valve closures, but the generation mechanism and components of these radial pressure waves are not clear from their study. Therefore, it is important to investigate the generation mechanism and components of radial pressure waves excited in viscous and initially non-static flows under various valve operations, which is the main scope of this research.

This study first addresses the inefficiency problem of the original Mitra-Rouleau scheme by: (i) transforming the original scheme into tridiagonal systems; and (ii) implementing non-uniform computational grids. The modified efficient scheme is then

extended into a typical RPV system to simulate a water hammer event. The efficient model is validated by numerical data from the analytical 1D Zielke's model, which has been extensively confirmed by lab experiments [11, 33, 34]. Afterwards, the modified and validated full-2D model is used to investigate systematically the radial pressure wave behavior in transient laminar pipe flows under different flow perturbations induced by various valve operations. Particularly, the generation mechanism and detailed components of radial pressure waves are studied and examined in this study. Finally, the findings and practical implications of this research are discussed at the end of this paper.

MODELS AND METHODS

Full-2D Water Hammer Model Derivation

The 2D non-conservative form Navier-Stokes equations for a compressible Newtonian fluid in axis symmetric flow field, written in a cylindrical coordinate system [4], are as follows,

$$\frac{\partial \rho}{\partial t} + u' \frac{\partial \rho}{\partial x} + v' \frac{\partial \rho}{\partial r} + \rho \left(\frac{\partial u'}{\partial x} + \frac{\partial v'}{\partial r} + \frac{v'}{r} \right) = 0 \tag{1a}$$

$$\rho \left(\frac{\partial u'}{\partial t} + u' \frac{\partial u'}{\partial x} + v' \frac{\partial u'}{\partial r} \right) = -\frac{\partial p'}{\partial x} + (\kappa + \mu/3) \frac{\partial}{\partial x} \left(\frac{\partial u'}{\partial x} + \frac{1}{r} \frac{\partial (rv')}{\partial r} \right) + \mu \left(\frac{\partial^2 u'}{\partial x^2} + \frac{1}{r} \frac{\partial}{\partial r} \left(r \frac{\partial u'}{\partial r} \right) \right) + \rho F_x \tag{1b}$$

$$\rho \left(\frac{\partial v'}{\partial t} + u' \frac{\partial v'}{\partial x} + v' \frac{\partial v'}{\partial r} \right) = -\frac{\partial p'}{\partial r} + (\kappa + \mu/3) \frac{\partial}{\partial r} \left(\frac{\partial u'}{\partial x} + \frac{1}{r} \frac{\partial (rv')}{\partial r} \right) + \mu \left(\frac{\partial^2 v'}{\partial x^2} + \frac{1}{r} \frac{\partial}{\partial r} \left(r \frac{\partial v'}{\partial r} \right) - \frac{v'}{r^2} \right) + \rho F_r \tag{1c}$$

where t = time; x = axial coordinate along pipe centerline; r = radial coordinate from pipe centerline; ρ = fluid density; u' = axial velocity; v' = radial velocity; p' = pressure; μ

= dynamic viscosity; κ = volume viscosity; F_x = body force along x; F_r = body force along r.

To derive the full-2D water hammer model from Eqs. (1), two assumptions are made herein:

(1) In classic water hammer problems, the compressibility of the fluid (water) is only considered in the continuity equation Eq. (1a). Since water is slightly compressible and the pipe wall is rigid in this study, the spatial variation of fluid density ρ in radial and axial momentum equations due to the spatial variation of internal pressure can be neglected. Meanwhile, the volume viscosity can also be neglected due to this slight compressibility of fluid (i.e., water) for this investigation. However, the small spatial variation of fluid density ρ in continuity equation should be included since the value of wave speed a_0 is finite. The equation of state for a slightly compressible fluid is [30]

$$\frac{dp'}{d\rho} = \frac{k}{\rho} = a_0^2 \tag{2}$$

where a_0 = wave speed; k = bulk modulus.

(2) The body forces F_x and F_r are negligible due to the relatively small scales of pipe size and pipeline gradient in UWSS focused in this study [1, 4, 5, 30].

These two assumptions reduce Eqs. (1) to

$$\frac{\partial p'}{\partial t} + u'\frac{\partial p'}{\partial x} + v'\frac{\partial p'}{\partial r} + k\left(\frac{\partial u'}{\partial x} + \frac{\partial v'}{\partial r} + \frac{v'}{r}\right) = 0 \tag{3a}$$

$$\frac{\partial u'}{\partial t} + u'\frac{\partial u'}{\partial x} + v'\frac{\partial u'}{\partial r} = -\frac{1}{\rho_0}\frac{\partial p'}{\partial x} + \frac{\mu}{\rho_0}\left(\frac{4}{3}\frac{\partial^2 u'}{\partial x^2} + \frac{1}{r}\frac{\partial}{\partial r}\left(r\frac{\partial u'}{\partial r}\right) + \frac{1}{3}\frac{\partial}{\partial x}\left(\frac{1}{r}\frac{\partial\left(rv'\right)}{\partial r}\right)\right) \tag{3b}$$

$$\frac{\partial v'}{\partial t}+u'\frac{\partial v'}{\partial x}+v'\frac{\partial v'}{\partial r}=-\frac{1}{\rho_0}\frac{\partial p'}{\partial r}+\frac{\mu}{\rho_0}\left(\frac{1}{3}\frac{\partial^2 u'}{\partial x\partial r}+\frac{\partial^2 v'}{\partial x^2}+\frac{4}{3}\frac{\partial}{\partial r}\left(\frac{1}{r}\frac{\partial\left(rv'\right)}{\partial r}\right)\right) \tag{3c}$$

where ρ_0 = mean density of the fluid (water).

In this study, the above full-2D model is further expressed in dimensionless form so as to inspect the principle and physics behind the problem with more general results. The chosen dimensionless variables are as follows [30]: $u = u'/u_0$, where u_0 is the initial average axial velocity; $v = v'/u_0$; $p = (p' - p_e')/\rho_0 u_0 a_0$, where p_e' = pressure at $x = 0$; $\tau = a_0 t/R$, where R = pipe radius; $\xi = x/R$; $\eta = r/R$. This results in the following dimensionless full-2D model,

$$\frac{\partial p}{\partial \tau}+\frac{\partial u}{\partial \xi}+\frac{\partial v}{\partial \eta}+\frac{v}{\eta}=-\mathbf{M}\left(u\frac{\partial p}{\partial \xi}+v\frac{\partial p}{\partial \eta}\right) \tag{4a}$$

$$\frac{\partial u}{\partial \tau}+\frac{\partial p}{\partial \xi}=-\mathbf{M}\left(u\frac{\partial u}{\partial \xi}+v\frac{\partial u}{\partial \eta}\right)+\mathbf{K}\left[\frac{4}{3}\frac{\partial^2 u}{\partial \xi^2}+\frac{1}{\eta}\frac{\partial}{\partial \eta}\left(\eta\frac{\partial u}{\partial \eta}\right)+\frac{1}{3}\frac{\partial}{\partial \xi}\left(\frac{1}{\eta}\frac{\partial}{\partial \eta}(\eta v)\right)\right] \tag{4b}$$

$$\frac{\partial v}{\partial \tau}+\frac{\partial p}{\partial \eta}=-\mathbf{M}\left(u\frac{\partial v}{\partial \xi}+v\frac{\partial v}{\partial \eta}\right)+\mathbf{K}\left[\frac{1}{3}\frac{\partial^2 u}{\partial \xi\partial \eta}+\frac{\partial^2 v}{\partial \xi^2}+\frac{4}{3}\frac{\partial}{\partial \eta}\left(\frac{1}{\eta}\frac{\partial}{\partial \eta}(\eta v)\right)\right] \tag{4c}$$

where $\mathbf{M} = u_0/a_0$ is the Mach number; $\mathbf{K} = \mu/R\rho_0 a_0$.

Original Mitra-Rouleau Scheme

Mitra and Rouleau [30] numerically solved the full-2D model in Eqs. (4) by an implicit matrix factorization method. In water hammer applications, the values of factors $\mathbf{M}$ and $\mathbf{K}$ on the right-hand side (RHS) of Eqs. (4) are negligibly small compared with one unit (i.e., $\mathbf{M} << 1$ and $\mathbf{K} << 1$); thus, terms on the RHS of Eqs. (4) were handled explicitly and terms on the left-hand side (LHS) were handled implicitly. The time derivatives on the LHS of Eqs. (4) were discretized by the three-point backward

difference given by $(\partial Z/\partial\tau)^{n+1} = (3Z^{n+1} - 4Z^n + Z^{n-1})/2\Delta\tau$, where $Z = p$, u or v; $\Delta\tau$ = size of time step; n = n-th time step; and $Z(\tau, \xi, \eta) = Z(n\Delta\tau, \xi, \eta) = Z^n(\xi, \eta)$. By expressing the RHS of Eqs. (4) as R_1, R_2 and R_3, Eqs. (4) were written in matrix form $\mathbf{ax} = \mathbf{b}$ as

$$\begin{bmatrix} 1 & \frac{2}{3}\Delta\tau\frac{\partial}{\partial\xi} & \frac{2}{3}\Delta\tau\left(\frac{\partial}{\partial\eta}+\frac{1}{\eta}\right) \\ \frac{2}{3}\Delta\tau\frac{\partial}{\partial\xi} & 1 & 0 \\ \frac{2}{3}\Delta\tau\frac{\partial}{\partial\eta} & 0 & 1 \end{bmatrix} \begin{bmatrix} p^{n+1} \\ u^{n+1} \\ v^{n+1} \end{bmatrix} = \begin{bmatrix} \frac{4}{3}p^n - \frac{1}{3}p^{n-1} + \frac{2}{3}\Delta\tau R_1^n \\ \frac{4}{3}u^n - \frac{1}{3}u^{n-1} + \frac{2}{3}\Delta\tau R_2^n \\ \frac{4}{3}v^n - \frac{1}{3}v^{n-1} + \frac{2}{3}\Delta\tau R_3^n \end{bmatrix} \tag{5}$$

where $\mathbf{a}$ = coefficient matrix; $\mathbf{x}$ = unknown vector consisting of variables at time step n+1; $\mathbf{b}$ = known vector consisting of variables at time steps n and n–1. Then the coefficient matrix $\mathbf{a}$ in Eq. (5) was approximately split into two individual coefficient matrixes

$$\mathbf{a} \approx \mathbf{a}_\xi \mathbf{a}_\eta \tag{6}$$

where $\mathbf{a}_\xi$ = coefficient matrix in the ξ-direction; $\mathbf{a}_\eta$ = coefficient matrix in the η-direction. $\mathbf{a}_\xi$ and $\mathbf{a}_\eta$ are in the following form [30]

$$\mathbf{a}_\xi = \begin{bmatrix} 1 & \frac{2}{3}\Delta\tau\frac{\partial}{\partial\xi} & 0 \\ \frac{2}{3}\Delta\tau\frac{\partial}{\partial\xi} & 1 & 0 \\ 0 & 0 & 1 \end{bmatrix}; \quad \mathbf{a}_\eta = \begin{bmatrix} 1 & 0 & \frac{2}{3}\Delta\tau\left(\frac{\partial}{\partial\eta}+\frac{1}{\eta}\right) \\ 0 & 1 & 0 \\ \frac{2}{3}\Delta\tau\frac{\partial}{\partial\eta} & 0 & 1 \end{bmatrix}.$$

Substituting Eq. (6) into Eq. (5), it became

$$\mathbf{a}_\xi \mathbf{a}_\eta \mathbf{x} = \mathbf{b} \tag{7}$$

A two-step algorithm was used to determine the unknown variables p^{n+1}, u^{n+1} and v^{n+1} in the vector $\mathbf{x}$. Firstly, they swept in the ξ-direction and solved Eq. (8) to get $\mathbf{x}^*$.

$$\mathbf{a}_{\xi}\mathbf{x}^{*}=\mathbf{b} \tag{8}$$

where $\mathbf{x}^{*}$ = ($p^{*\,n+1}$, $u^{*\,n+1}$, $v^{*\,n+1}$)$^{\mathrm{T}}$ was an intermediate vector, in which $p^{*\,n+1}$, $u^{*\,n+1}$ and $v^{*\,n+1}$ were intermediate variables. Secondly, they swept in the η-direction and solved Eq. (9) to get the unknown vector $\mathbf{x}$ = (p^{n+1}, u^{n+1}, v^{n+1})$^{\mathrm{T}}$.

$$\mathbf{a}_{\eta}\mathbf{x}=\mathbf{x}^{*} \tag{9}$$

In this way, the 2D problem was decomposed into two 1D problems, which reduced the computational burden. The spatial derivatives in $\mathbf{a}_{\xi}$ and $\mathbf{a}_{\eta}$ of Eqs. (8) and (9) were approximated by the upwind scheme.

The whole flow field was spatially discretized into I and J uniform sections in the ξ- and η- directions, respectively. Donating the known vector $\mathbf{b}$ on the RHS of Eq. (5) as $\mathbf{b}$ = ($T_1^{\,n}$, $T_2^{\,n}$, $T_3^{\,n}$)$^{\mathrm{T}}$, for an arbitrary cross in the flow field (ξ, η) = ($i\Delta\xi$, $j\Delta\eta$), Eq. (8) could be expressed as

$$-\frac{1}{3}\frac{\Delta\tau}{\Delta\xi}u_{i-1,j}^{*n+1}-\frac{1}{3}\frac{\Delta\tau}{\Delta\xi}p_{i-1,j}^{*n+1}+0u_{i,j}^{*n+1}+\left(1+\frac{2}{3}\frac{\Delta\tau}{\Delta\xi}\right)p_{i,j}^{*n+1}+\frac{1}{3}\frac{\Delta\tau}{\Delta\xi}u_{i+1,j}^{*n+1}-\frac{1}{3}\frac{\Delta\tau}{\Delta\xi}p_{i+1,j}^{*n+1}=\left(T_1^{\,n}\right)_{i,j} \tag{10a}$$

$$-\frac{1}{3}\frac{\Delta\tau}{\Delta\xi}u_{i-1,j}^{*n+1}-\frac{1}{3}\frac{\Delta\tau}{\Delta\xi}p_{i-1,j}^{*n+1}+\left(1+\frac{2}{3}\frac{\Delta\tau}{\Delta\xi}\right)u_{i,j}^{*n+1}+0\,p_{i,j}^{*n+1}-\frac{1}{3}\frac{\Delta\tau}{\Delta\xi}u_{i+1,j}^{*n+1}+\frac{1}{3}\frac{\Delta\tau}{\Delta\xi}p_{i+1,j}^{*n+1}=\left(T_2^{\,n}\right)_{i,j} \tag{10b}$$

$$v_{i,j}^{*n+1}=\left(T_3^{\,n}\right)_{i,j} \tag{10c}$$

where $\Delta\xi$ = spatial step in the ξ-direction; $\Delta\eta$ = spatial step in the η-direction; i = i-th spatial step in the ξ-direction; j = j-th spatial step in the η-direction.

Similarly, for the cross located at ($i\Delta\xi$, $j\Delta\eta$), Eq. (9) could be written as

$$-\frac{1}{3}\frac{\Delta\tau}{\Delta\eta}v_{i,j-1}^{n+1}-\frac{1}{3}\frac{\Delta\tau}{\Delta\eta}p_{i,j-1}^{n+1}+\frac{2}{3}\frac{\Delta\tau}{(j-1)\Delta\eta}v_{i,j}^{n+1}+\left(1+\frac{2}{3}\frac{\Delta\tau}{\Delta\eta}\right)p_{i,j}^{n+1}+\frac{1}{3}\frac{\Delta\tau}{\Delta\eta}v_{i,j+1}^{n+1}-\frac{1}{3}\frac{\Delta\tau}{\Delta\eta}p_{i,j+1}^{n+1}=p_{i,j}^{*n+1} \tag{11a}$$

$$u_{i,j}^{n+1}=u_{i,j}^{*n+1} \tag{11b}$$

$$-\frac{1}{3}\frac{\Delta\tau}{\Delta\eta}v_{i,j-1}^{n+1}-\frac{1}{3}\frac{\Delta\tau}{\Delta\eta}p_{i,j-1}^{n+1}+\left(1+\frac{2}{3}\frac{\Delta\tau}{\Delta\eta}\right)v_{i,j}^{n+1}+0\,p_{i,j}^{n+1}-\frac{1}{3}\frac{\Delta\tau}{\Delta\eta}v_{i,j+1}^{n+1}+\frac{1}{3}\frac{\Delta\tau}{\Delta\eta}p_{i,j+1}^{n+1}=v_{i,j}^{*n+1} \tag{11c}$$

Therefore, the governing equations at fixed (j, n+1) for all inner points along the ξ-direction (i.e., i ranges from 2 to I–1) could be written in matrix form as $\mathbf{A}_\xi\mathbf{X}^*=\mathbf{B}$, where $\mathbf{X}^*=[(u^{*n+1})_{1,j},(p^{*n+1})_{1,j},\ldots,(u^{*n+1})_{i,j},(p^{*n+1})_{i,j},\ldots,(u^{*n+1})_{I,j},(p^{*n+1})_{I,j}]^{\mathrm{T}}$ = unknown vector; $\mathbf{B}=[(T_1{}^n)_{2,j},(T_2{}^n)_{2,j},\ldots,(T_1{}^n)_{i,j},(T_2{}^n)_{i,j},\ldots,(T_1{}^n)_{I\text{-}1,j},(T_2{}^n)_{I\text{-}1,j}]^{\mathrm{T}}$ = known vector; $\mathbf{A}_\xi$ is a coefficient matrix in the following form

$$\begin{pmatrix}
-\frac{E}{2} & -\frac{E}{2} & 0 & F & \frac{E}{2} & -\frac{E}{2} & & & & \cdots & & & & 0\\
-\frac{E}{2} & -\frac{E}{2} & F & 0 & -\frac{E}{2} & \frac{E}{2} & & & & & & & & \\
 & & -\frac{E}{2} & -\frac{E}{2} & 0 & F & \frac{E}{2} & -\frac{E}{2} & & & & & & \\
 & & -\frac{E}{2} & -\frac{E}{2} & F & 0 & -\frac{E}{2} & \frac{E}{2} & & & & & & \\
0 & & & & \cdots & \cdots & \cdots & \cdots & & & & & & \\
 & & & & & & & & \cdots & \cdots & \cdots & \cdots & & 0\\
 & & & & & & & & -\frac{E}{2} & -\frac{E}{2} & 0 & F & \frac{E}{2} & -\frac{E}{2}\\
 & & & & & & & & -\frac{E}{2} & -\frac{E}{2} & F & 0 & -\frac{E}{2} & \frac{E}{2}\\
 & & & & & & & & & & -\frac{E}{2} & -\frac{E}{2} & 0 & F\\
0 & & & & \cdots & & & & & & -\frac{E}{2} & -\frac{E}{2} & F & 0
\end{pmatrix} \tag{12}$$

where E = 2/3($\Delta\tau/\Delta\xi$); F = 1 + 2/3($\Delta\tau/\Delta\xi$).

Similarly, the governing equations at fixed (i, n+1) for all inner points along the η-direction (i.e., j ranges from 2 to J–1) could be written in matrix form as $\mathbf{A}_\eta\mathbf{X}=\mathbf{X}^*$, where $\mathbf{X}=[(v^{n+1})_{i,1},(p^{n+1})_{i,1},\ldots,(v^{n+1})_{i,j},(p^{n+1})_{i,j},\ldots,(v^{n+1})_{i,J},(p^{n+1})_{i,J}]^{\mathrm{T}}$ = unknown vector; $\mathbf{A}_\eta$ is a coefficient matrix in the following form

$$\begin{pmatrix}
-\frac{Z}{2} & -\frac{Z}{2} & V_2 & Y & \frac{Z}{2} & -\frac{Z}{2} & & & & \cdots & & & & 0\\
-\frac{Z}{2} & -\frac{Z}{2} & Y & 0 & -\frac{Z}{2} & \frac{Z}{2} & & & & & & & & \\
 & & -\frac{Z}{2} & -\frac{Z}{2} & V_3 & Y & \frac{Z}{2} & -\frac{Z}{2} & & & & & & \\
 & & -\frac{Z}{2} & -\frac{Z}{2} & Y & 0 & -\frac{Z}{2} & \frac{Z}{2} & & & & & & \\
0 & & & & \cdots & \cdots & \cdots & \cdots & & & & & & \\
 & & & & & & & & \cdots & \cdots & \cdots & \cdots & & 0\\
 & & & & & & & & -\frac{Z}{2} & -\frac{Z}{2} & V_{J-2} & Y & \frac{Z}{2} & -\frac{Z}{2}\\
 & & & & & & & & -\frac{Z}{2} & -\frac{Z}{2} & Y & 0 & -\frac{Z}{2} & \frac{Z}{2}\\
 & & & & & & & & & & -\frac{Z}{2} & -\frac{Z}{2} & V_{J-1} & Y\\
0 & & & & \cdots & & & & & & -\frac{Z}{2} & -\frac{Z}{2} & Y & 0
\end{pmatrix} \tag{13}$$

where $Z = 2/3(\Delta\tau/\Delta\eta)$; $Y = 1 + 2/3(\Delta\tau/\Delta\eta)$; $V_j = 2/3(\Delta\tau/(j-1)\Delta\eta)$.

Although the 2D problem has been decomposed into two 1D problems, the original Mitra-Rouleau scheme is still computationally intensive due to the complexity of the two coefficient matrixes in Eqs. (12) and (13). Moreover, it is not convenient and practical to capture detailed physics in the boundary layer near the pipe wall by uniform grids along the radial direction (from pipe centerline to pipe wall) implemented in the original Mitra-Rouleau scheme.

Modified Mitra-Rouleau Scheme

Inspired by the previous work of Zhao and Ghidaoui [8], the efficiency of existing scheme for the full-2D model can be enhanced by transforming the original matrixes in Eqs. (12) and (13) to two tridiagonal matrixes in Eqs. (14) and (15), which can be solved by the LU factorization method efficiently. Meanwhile, the non-uniform computational grid (the grid size expressed as $\Delta\eta_j$) is also implemented along the radial direction to enhance the efficiency and reliability. In general, the application cases of this study demonstrate that, for the same expected accuracy and computer environment, compared with the original scheme, only about 1/6 of the CPU time and 1/2 of the computer memory are needed for the modified scheme.

$$\begin{pmatrix} \frac{2EF}{E^2-F^2} & 1 & \frac{F^2+E^2}{F^2-E^2} & & & & \cdots & & & & 0 \\ & \frac{F^2+E^2}{E^2-F^2} & 1 & \frac{2EF}{F^2-E^2} & & & & & & & \\ & & \frac{2EF}{E^2-F^2} & 1 & \frac{F^2+E^2}{F^2-E^2} & & & & & & \\ & & & \frac{F^2+E^2}{E^2-F^2} & 1 & \frac{2EF}{F^2-E^2} & & & & & \\ 0 & & & & \cdots & \cdots & \cdots & & & & \\ & & & & & \cdots & \cdots & \cdots & & & 0 \\ & & & & & & \frac{2EF}{E^2-F^2} & 1 & \frac{F^2+E^2}{F^2-E^2} & & \\ & & & & & & & \frac{F^2+E^2}{E^2-F^2} & 1 & \frac{2EF}{F^2-E^2} & \\ & & & & & & & & \frac{2EF}{E^2-F^2} & 1 & \frac{F^2+E^2}{F^2-E^2} \\ 0 & & & & \cdots & & & & & \frac{F^2+E^2}{E^2-F^2} & 1 & \frac{2EF}{F^2-E^2} \end{pmatrix} \tag{14}$$

$$\begin{pmatrix} \frac{YZ-W_1Z}{W_1X_2+Z^2} & 1 & \frac{W_1Y-Z^2}{W_1X_2+Z^2} & & & & \cdots & & & & 0 \\ & \frac{W_2Y-Z^2}{Y^2-Z^2} & 1 & \frac{YZ+X_3Z}{Y^2-Z^2} & & & & & & & \\ & & \frac{YZ-W_2Z}{W_2X_3+Z^2} & 1 & \frac{W_2Y-Z^2}{W_2X_3+Z^2} & & & & & & \\ & & & \frac{W_3Y-Z^2}{Y^2-Z^2} & 1 & \frac{YZ+X_4Z}{Y^2-Z^2} & & & & & \\ 0 & & & & \cdots & \cdots & \cdots & & & & \\ & & & & & \cdots & \cdots & \cdots & & & 0 \\ & & & & & & \frac{YZ-W_{J-3}Z}{W_{J-3}X_{J-2}+Z^2} & 1 & \frac{W_{J-3}Y-Z^2}{W_{J-3}X_{J-2}+Z^2} & & \\ & & & & & & & \frac{W_{J-2}Y-Z^2}{Y^2-Z^2} & 1 & \frac{YZ+X_{J-1}Z}{Y^2-Z^2} & \\ & & & & & & & & \frac{YZ-W_{J-2}Z}{W_{J-2}X_{J-1}+Z^2} & 1 & \frac{W_{J-2}Y-Z^2}{W_{J-2}X_{J-1}+Z^2} \\ 0 & & & & \cdots & & & & & \frac{W_{J-1}Y-Z^2}{Y^2-Z^2} & 1 & \frac{YZ+X_JZ}{Y^2-Z^2} \end{pmatrix} \tag{15}$$

where $W_j = 2/3(\Delta\tau/\eta_j) - 1 - 2/3(\Delta\tau/\Delta\eta_j)$; $X_j = 1 + 2/3(\Delta\tau/\Delta\eta_j) + 2/3(\Delta\tau/\eta_j)$.

Initial and Boundary Conditions

Then the modified Mitra-Rouleau scheme is extended into a RPV experimental system (Fig. 1), with following initial and boundary conditions

Initial Conditions

The initial flow ($\tau = 0$) in the pipe is a Poiseuille laminar flow. The initial values for the axial velocity u, radial velocity v and pressure p are given below

$$u = 2\left(\eta^2 - 1\right); v = 0;\ p = 8\mathbf{K}\xi \tag{16}$$

The initial axial velocity profile along the pipe radius and the area-averaged velocity is plotted in Fig. 2.

Boundary Conditions

The no-slip condition at the pipe wall (η = 1) is

$$u = 0;\ v = 0;\ \frac{\partial p}{\partial \eta} = R_3 \tag{17}$$

The symmetry condition at the pipe centerline (η = 0) is

$$\frac{\partial u}{\partial \eta} = 0;\ v = 0;\ \frac{\partial p}{\partial \eta} = 0 \tag{18}$$

The upstream reservoir ($\xi = I\Delta\xi$) with constant pressure

$$\frac{\partial u}{\partial \xi} = R_1;\ v = 0;\ p = 8\mathbf{K}\xi \tag{19}$$

Different Operations on the Downstream Valve

To generate transients, the downstream valve is operated in the following two patterns:

(i) Sudden valve closure

$$u = 2\left(\eta^2 - 1\right) \text{ when } \tau = 0;\ \ u = 0 \text{ when } \tau > 0;\ \ \frac{\partial p}{\partial \xi} = -\frac{\partial u}{\partial \tau} + R_2 \tag{20}$$

(ii) Valve oscillation with frequency f_{in}

$$u = 0.5\left[2\left(\eta^2 - 1\right)\right]\left[\cos\left(2\pi f_{in}\tau\right) + 1\right] \text{ when } \tau < \tau_0;\ \ u = 0 \text{ when } \tau > \tau_0;\ \ \frac{\partial p}{\partial \xi} = -\frac{\partial u}{\partial \tau} + R_2 \tag{21}$$

where τ_0 = time duration of the valve oscillation.

MODEL VERIFICATION AND NUMERICAL VALIDATION

The validity of the present code is firstly examined by numerical data from [30]. Detailed system parameters of this numerical experiment are listed in Table 1. Note that the reflection-free condition is applied to the upstream boundary. An initial Poiseuille

laminar flow in the pipe is stopped by a downstream valve (at ξ = 0) closure with closing time τ_0 = 0.4. The pressure history at the valve for three different radial points is plotted in Fig. 3. A good agreement can be observed between numerical data from the present code and [30].

The modified scheme is further extended into a classical RPV water hammer experimental system (Fig. 1). Initially, keeping the downstream valve fully open, a steady laminar flow with average axial velocity u_0 is formed in the pipe. As mentioned, transients are caused by various operations on the downstream valve.

Model Verification (Grid Independence Tests)

In the modified Mitra-Rouleau scheme, uniform and non-uniform spatial grids are adopted in the ξ- and η- directions, respectively. In transient pipe flows, the high-resolution grid is essential for the finite difference scheme to accurately calculate hydraulic variables. For this purpose, three different grid sizes, as shown in Table 2, are tested to verify the modified full-2D model, in which N_r is the number of non-uniform grid along the radial direction. The upstream boundary is a reservoir with constant pressure (i.e., Eq. (19)).

As shown in Fig. 1, transients are caused by a typical operation of sudden downstream valve closure. Then pressure along the pipe radius (termed as radial pressure) is measured at the valve and the mid-length of the pipe. The area-averaged pressure traces are calculated and plotted in Fig. 4. As shown in Fig. 4, the pressure is normalized by the steady state pressure head at the downstream valve and the time is normalized by the system theoretical period $T_{th} = 4L/a_0$. The pressure gets convergence

as the mesh becomes finer. The result of N_r = 80 demonstrates sufficient accuracy; thus, it will be chosen as the computational grid in the numerical validation.

Numerical Validation

The analytical 1D Zielke's and quasi-2D models for transient laminar flows have been widely validated by experimental tests in the literature, for their capability of capturing area-averaged pressure head traces [6, 10, 11]. But the two-dimensionality of transient pipe flows has not yet well verified due to the difficulty of measuring two-dimensional data in experimental tests. Therefore, the modified full-2D model of this study is validated herein by the 1D Zielke's model for modeling the area-averaged transient pressure head. Afterwards, the radial pressure waves in transient laminar pipe flows are analyzed based on the validated full-2D model in the numerical applications.

Transients are caused by a sudden downstream valve closure; then radial pressure is measured at the valve and the mid-length of the pipe to calculate the area-averaged pressure. The area-averaged pressure trace of the full-2D model is plotted in Fig. 5. Good agreement between the full-2D model and Zielke's model in both pressure amplitude and pressure phase can be observed in Fig. 5. This demonstrates the validity of the present full-2D model for modelling transient laminar pipe flows.

NUMERICAL APPLICATIONS

The validated full-2D model is applied to a RPV system (Fig. 1) to investigate the generation mechanism and components of radial pressure waves. Three tests are conducted, in which transients (fast flow perturbations) are caused by different

operations on the downstream valve (specifically, sudden closure for Test 1, low frequency perturbation for Test 2, and high frequency perturbation for Test 3). Actually, the definitions of low frequency flow perturbation and high frequency flow perturbation are system dependent, which will be clarified later for the case study. For the study of UWSS, the fluid used in this part is water and the wave speed a_0 is assumed to be 1485 m/s for relatively rigid pipes [1]. The initial condition in the pipe is a Poiseuille flow with $\mathrm{Re} = 100$ (Eq. (16) and Fig. 2).

Because the following results involve high radial modes, there is a need to review related fundamental theory herein. Louati and Ghidaoui [31] showed that the radial wave number k_{rm} for a water-filled pipe can be determined by the no-flux boundary condition at the pipe wall $J_1(\alpha_{rm}) = 0$, where $\alpha_{rm} = k_{rm}R$; J_1 is the Bessel function of first kind of order 1. $J_1(\alpha_{rm}) = 0$ gives $\alpha_{rm} = 0$, 3.83171, 7.01559, 10.17347, …, etc, then the radial wave number k_{rm} ($k_{rm} = \alpha_{rm}/R$) and cut-off frequency f_m ($f_m = a_0 k_{rm}/2\pi$) of the m-th radial mode can be calculated accordingly. The group velocity V_{gm} of m-th radial mode is given by Eq. (22) and the result for the test system in Table 3 is plotted in Fig. 6 [31]. For simplicity of illustration, these high radial modes are defined as mode 1 (M1), mode 2 (M2), etc., in the following study.

$$V_{gm} = \frac{a\sqrt{(\omega/a)^2 - k_{rm}^2}}{\omega/a} \tag{22}$$

Flow Perturbation by Sudden Valve Closure

For Test 1 in Table 3, transients are caused by a sudden and complete downstream valve (at $\xi = 0$) closure at time 0. The temporal variations of pressure at the

valve for two radial locations, at the pipe axis p_{axis} (at η = 0) and pipe wall p_{wall} (at η = 1), are plotted in Fig. 7. Note that the area-averaged pressure p_{avg} at the valve is plotted for convenient comparison. To intuitively observe the spatial variation of pressure in the radial direction (validity of the plane wave assumption), the pressure difference Δp between the pipe axis and wall (Eq. (23)) is also plotted in Fig. 7.

$$\Delta p = p_{axis} - p_{wall} \tag{23}$$

Fig. 7 shows that the worst-case moment for the plane wave assumption (i.e., largest value of radial pressure difference Δp) is observed at time 0 when the valve is suddenly closed. The pressure at the pipe wall p_{wall} remains 0.0 and the pressure at the pipe axis p_{axis} leaps to its peak value of 2.0, which is twice the area-averaged pressure p_{avg}. This is due to the velocity profile of the initial Poiseuille laminar flow. As shown in Fig. 2, the velocities at the pipe axis and pipe wall as well as area-averaged velocity are 2, 0 and 1, respectively. When the valve is closed at time 0, all the three velocities are reduced to 0. Based on the normalized Joukowsky's equation [35], $\Delta p = -\Delta u/u_0$, the p_{axis}, p_{wall} and p_{avg} should become 2, 0 and 1, respectively. Because of the existence of the relative large pressure variation within the pipe cross section, the radial flux (or radial velocity) is formed, and so is the radial pressure waves. Afterwards, both pressure curves (p_{axis} and p_{wall}) fluctuate with decreasing amplitude due to the existence of the viscosity.

It is also noticed that no matter how the radial pressure changes at the valve, the area-averaged pressure (black curve in Fig. 7) maintains the constant value of 1.0, which is exactly the equivalent pressure information that 1D and quasi-2D models can only obtain.

The radial pressure profiles at nine time points (i.e., denoted as t_1 ~ t_9) within one period of the pressure fluctuation, as shown in the enlarged view of Fig. 7, are selected and plotted in Fig. 8(a). Fig. 8(a) shows that there are two pressure antinodes, where the radial pressure fluctuation has the maximum amplitude, locating at the pipe axis (at η = 0.0) and pipe wall (at η = 1.0). Moreover, a pressure node is observed at η = 0.625, which agrees well with the theoretical result of the node location $\eta \approx 0.627$ of $\mathrm{M}1$ for this studied case [31, 32].

To gain an insight into the components of radial pressure waves caused by a sudden valve closure, the time domain signal in Fig. 7 is transformed into the frequency domain by a fast Fourier transform (FFT) algorithm shown in Fig. 8(b). For clarity, the amplitude in Fig. 8(b) is plotted in a logarithmic coordinate. Fig. 8(b) shows that the first four frequency peaks of radial pressure waves are 4454, 8315, 12180 and 15740, which are consistent with the theoretical cut-off frequency of first four high radial modes in Fig. 6 (i.e., 4528, 8291, 12022 and 15745 by Eq. (22)) [31, 32]. Note that the group velocity for radial pressure waves in cut-off frequency should be 0 (Fig. 6), which means that the pressure signals (Fig. 7) measured at the valve would be the superposition of several radial standing waves. According to Fig. 8(b), most of the energy is distributed in the frequency mode of 4454 (i.e., $\mathrm{M}1$), which also results in the pressure node location at η = 0.625.

Furthermore, the temporal variations of pressure at mid-length of the pipe (i.e., at ξ = 25) are plotted in Fig. 9. According to Fig. 9, the wave front arrives at the mid-length at time $0.125T_{th}$. Shortly after the wave front, the pressure difference

between the pipe axis and pipe wall (i.e., Δp) is approximately equals to 0. To explain this, the velocity profiles at the mid-length before (i.e., at $0.120T_{th}$) and after (i.e., at $0.130T_{th}$) the wave front are plotted in Fig. 10. The result clearly shows that the passage of the wave front almost induces a uniform shift in velocity profile across the pipe radius [36]. Based on the Joukowsky's equation [35], the pressure along the pipe radius should uniformly jump to 1; and therefore, the wave shortly after the wave front is a plane wave and no localized high radial modes are excited. As shown in Fig. 9, this plane wave is followed by high radial modes (i.e., waves after $0.130T_{th}$). These high radial modes propagating from the downstream valve, with group velocity $V_{gn} < a_0$ (Fig. 6), should arrive later than the wave front (wave dispersion).

Low Frequency Flow Perturbation by Valve Oscillations

For Test 2 in Table 3, transients are generated by periodically oscillating the downstream valve (at $\xi = 0$). During such valve oscillation process, the axial velocity profile at the valve is given as $u_1 = 0.5\cdot[2(\eta^2-1)]\cdot[\cos(2\pi f_{in1}\tau)+1]$ (i.e., Eq. (21)), where f_{in1} is the induced flow perturbation (i.e., valve oscillation) frequency. The ratio of f_{in1} to f_r is 0.2, i.e., $f_{in1}/f_r = 0.2 < 1$, which is defined as low frequency flow perturbation in this study. The duration of this perturbation process is $0.125T_{th}$.

To inspect, the temporal variations of pressure at the valve are plotted in Fig. 11, which reveals that the pressure difference between pipe axis and pipe wall (Δp) changes periodically during the valve oscillation. The radial pressure profiles for nine time points (i.e., t_1 ~ t_9) within one period of the valve oscillation, as shown in the left enlarged view of Fig. 11, is plotted in Fig. 12(a). As is shown in Fig. 12(a), the pressure variation along

the radial direction is quite evident. The pressure signal during the valve oscillation is transformed into the frequency domain in Fig. 12(b) by a FFT algorithm. The largest frequency peak with the value of 1485, which contains the most energy, is the frequency of the periodic valve oscillation (f_{in1} = 0.2f_r = 1485 Hz). In addition, the radial modes M1, M2 and M3 are also excited, but the energy carried by these high radial modes is relatively limited.

Similar to Test 1, according to Fig. 11, the plane wave assumption experiences the worst-case moment at time 0.125T_{th} when the valve is completely closed. The pressure at the pipe axis p_{axis} reaches its maximum value of 2.0, which is twice the area-averaged pressure p_{avg}. Then both local pressure curves (i.e., p_{axis} and p_{wall}) fluctuate periodically with amplitude damping. The pressure profiles for nine time points (i.e., t_1 ~ t_9) within one general fluctuation, as shown in the right enlarged view of Fig. 11, are selected and plotted in Fig. 13(a). It can be seen from Fig. 13(a) that the pressure node locates approximatively at η = 0.625. As is shown in Fig. 13(b), the pressure signal after the valve closure is also transformed into the frequency domain. Several high radial modes (i.e., M1, M2, M3 and M4) are motivated, but most of the energy is trapped in the M1, which can explain the location of the pressure node at η = 0.625 in Fig. 13(a).

Fig. 14 shows the temporal variations of pressure at the mid-length (i.e., ξ = 25) of the pipe. Similar with Test 1, no localized high radial modes are excited because the passage of the wave front uniformly changes the velocity profile along the pipe radius (like Fig. 10). According to Fig. 14, the signal, ranging from 0.125T_{th} to 0.25T_{th}, corresponding to valve-induced flow perturbation becomes a plane wave. This could be

attributed to the relatively limited energy carried by the high radial modes, with an order of 10^0 in comparison with the case of valve oscillation with an order of 10^3 (see Fig. 12(b)).

High Frequency Flow Perturbation by Valve Oscillations

For Test 3 in Table 3, the generation mechanism of transients is the same as Test 2 (i.e., periodic oscillation of the downstream valve), but with a relatively high frequency. The axial velocity profile at the valve is given by $u_2 = 0.5\cdot[2(\eta^2-1)]\cdot[\cos(2\pi f_{in2}\tau)+1]$, where f_{in2} is the valve oscillation frequency. In Test 3, f_{in2} equals to the radial wave frequency f_r, i.e., $f_{in1}/f_r = 1$, which is defined as high frequency flow perturbation in this study. The time duration of the valve operation is $0.125T_{th}$.

The variations of pressure with time at the valve are plotted in Fig. 15. According to Fig. 15, the pressure difference (Δp) between the pipe axis and pipe wall is much larger than that of Test 2. One reason for this is that the valve oscillation frequency (f_{in2}) is comparable to the radial wave frequency (f_r). Within one period of valve oscillation, there is no enough time for the radial wave to influence the whole pressure profile across the pipe cross section. Again, the radial pressure profiles for nine time points (i.e., t_1 ~ t_9), within one general period of valve oscillation, as shown in Fig. 15, are plotted in Fig. 16(a). This result shows that the pressure node and antinode locate at the pipe wall (η = 1.0) and pipe axis (η = 0.0), respectively. This can also be attributed to the relative high frequency of valve oscillation compared with radial wave frequency (f_r). The pressure signal during the valve oscillation is transformed into the frequency domain (Fig. 16(b)) by a FFT algorithm. It is shown in Fig. 16(b) that most of the energy is distributed

in the frequency of valve oscillation (i.e., 7425 Hz). Although the energy trapped in high frequency modes is still relatively limited, the value is now much larger than that of the Test 2.

In this test case, the valve is completely closed at time 0.125T_{th}. Unlike Test 1 and Test 2, both pressure curves (p_{aixs} and p_{wall}) fluctuate disorderly after the complete valve closure as shown in Fig. 15. The pressure profiles for nine time points within one general period, as shown in the enlarged view of Fig. 15, after the valve closure are plotted in Fig. 17(a). According to Fig. 17(a), it indicates that two pressure nodes (i.e., around η = 0.35 and 0.80) exist along the radial direction, which are close to the theoretical pressure node locations of M2 (i.e., $\eta \approx$ 0.343 and 0.787) [31]. To explore the components of radial pressure waves in Fig. 17(a), the pressure signal after the valve closure is transformed into the frequency domain and plotted in Fig. 17(b). The obtained result reveals that several high radial modes (i.e., M1, M2, M3 and M4) are excited. Moreover, the amplitude of M2 is comparable to the amplitude of M1. In other words, the energy almost trapped equally in M1 and M2. Therefore, both M1 and M2 are dominant among high radial modes. This can explain the disorder of both pressure curves (p_{axis} and p_{wall}) in Fig. 15 after the complete valve closure under the condition of high frequency valve oscillation.

The temporal variations of pressure at mid-length of the pipe (i.e., at ξ = 25) are plotted in Fig. 18. Similar with Test 1 and Test 2, no localized high radial modes are excited. However, the amplitude of the radial pressure waves, coming from the downstream valve, is larger than that of the Test 1 and Test 2. This is because more

energy is distributed into the high radial modes, which are now in an order of 10^1 or 10^2 for Test 3 in Fig. 16(b), during the valve oscillation.

RESULTS DISCUSSION

The results and findings above demonstrate that radial pressure waves can be excited by different operations on the downstream valve. A recent research conducted by Louati and Ghidaoui [31] has observed that radial pressure waves cannot be excited if the wave generator has the same diameter with the pipe. This is due to the inviscid and initially stagnant flow condition considered in [31]. Under such idealized flow condition, if the transient source size equals to the pipe diameter, the generated transient pressure will be independent of the pipe radius and propagate as a plane wave ($M0$). However, another generating mechanism of radial pressure waves has been identified for viscous and initially non-static flows in the present study, even though the downstream valve, having the same size as the pipe diameter, is used as the transient generator. That is, the non-uniform change in the initial velocity profile forms pressure gradients along the radial direction, which thereafter becomes the driving force of the formation of radial flux and radial pressure waves during transient flow process. In the practical UWSS, flows usually distribute with certain axial velocity profiles along the radial direction; thus, radial pressure waves caused by the non-uniform change in initial velocity profiles could occur and should also be considered in applications. From this perspective, the results of this study may be more close and useful to practical situations.

Furthermore, it has also shown that radial pressure waves may have very different behavior under different transient generation conditions (i.e., valve operations).

Specifically, for Test 1 with the typical operation of sudden and complete valve closure, high radial modes can be excited and most of the energy is carried by M1. As a result, a pressure node exists at η = 0.625 along the radial direction, which is useful to the better selection of pressure measurement locations during practical transient applications. For Test 2, during the relatively low frequency flow perturbation, the dominant energy is carried exactly by the valve oscillation (flow perturbation) frequency. After the complete valve closure at time $0.125T_{th}$, the amplitude of each excited high radial mode stays almost the same with Test 1. This implies that the valve oscillation with a low frequency of f_{in1} (e.g., $f_{in1} = 0.2f_r$ in this study) has a limited influence on the energy distribution among high radial modes. In Test 3, which is used for investigating the relatively high frequency flow perturbation, most of the energy is carried by the perturbation frequency during the valve oscillation. This is similar with Test 2. However, after the complete valve closure at time $0.125T_{th}$, the amplitude of M2 is almost identical to the M1 (see Fig. 17(b)), which indicates that the valve oscillation with the frequency of f_{in2} (i.e., $f_{in2} = 1.0f_r$) redistributes the energy among different high radial modes. Moreover, the pressure amplitude measured at the mid-length of the pipe is larger than that of Test 1 and Test 2.

The obtained results have also demonstrated that the maximum pressure (especially the local pressure at the pipe axis), caused by the fast valve closure or high frequency valve oscillation, can be much larger than the maximum pressure predicted by the 1D and quasi-2D models where a plane wave assumption is imposed. For viscous laminar pipe flows, the axial velocity is distributed parabolically along the radial

direction (i.e., Fig. 2) because of the no-slip boundary condition. The maximum velocity occurs at the pipe axis and it is twice the area-averaged velocity. The present full-2D model can give the true localized pressure variation along the radial direction. However, the pressure in the 1D and quasi-2D models can only be obtained from a perspective of the area-averaged quantity. Therefore, the traditional 1D and quasi-2D models might underestimate the destructive effects of the water hammer due to neglecting the influence of radial pressure waves during the complex transient process.

Consequently, the development and results of the efficient full-2D model in this study are useful to the design of qualified pipelines and related accessories for pipe system safety with regard to the pressure prediction, and to the utilization of transient waves for pipe diagnosis with regard to the selection and analysis of different wave modes and frequencies.

CONCLUSIONS

This paper investigates systematically the radial pressure wave behavior in transient laminar flows under different flow perturbations by valve operations. Firstly, the inefficiency problem of the current full-2D model has been addressed in this study by proposing a more efficient numerical scheme. Then the modified efficient full-2D model is extended into a RPV system to simulate the whole process of the water hammer, which is validated by the 1D analytical Zielke's model. With the efficient full-2D model, the generation mechanism and components of radial pressure waves excited by different valve operations are investigated extensively.

The obtained results have demonstrated that radial pressure waves can be induced from the non-uniform change in the initial velocity profile under valve operations, which forms pressure gradients along the radial direction. After transient generation, the existence of radial pressure gradients becomes the driving force of the formation of radial flux and radial pressure waves. This formation mechanism and results should be considered and included in the practical transient analysis (including transient design and utilization), since the flows in practical water piping systems are usually viscous and non-static. The results analysis also revealed that the generated radial pressure waves are composed of different high radial modes. Moreover, the valve-induced flow perturbations (with different frequencies) may influence the energy distribution among different high radial modes. Specifically, the results of this study indicate that most of the energy is carried by M1 for cases of flow perturbations by sudden valve closure and low frequency valve oscillation, while for high frequency flow perturbation, the energy is almost entrapped equally in M1 and M2.

From the results and findings of this study, it is demonstrated that the developed efficient full-2D model has made it possible to understand the radial pressure wave behavior in transient laminar pipe flows. This model may be useful to the design of qualified pipeline systems, as well as helpful to more accurate detection of defects (leakage and blockage) in pipelines. Finally, it is also noted that only initial laminar flows and valve-based transient generation are considered in current study, and further investigation will be required for turbulent flows and other complex transient phenomena in the future work.

ACKNOWLEDGEMENTS

This research work was supported by the research grants from: (1) the Hong Kong Research Grants Council (projects no. T21-602/15-R, no. 25200616 and no. 15201017); and (2) the Hong Kong Polytechnic University (projects no. 1-ZVCD and no. 1-ZVGF). In addition, the author Che would like to thank Dr. H.X. Yan from Tongji University for his technical suggestions.

NOMENCLATURE

a_0	wave speed
f_{in}	the valve oscillation frequency
f_r	radial wave frequency
F_r	body force along r
F_x	body force along x
I	total number of spatial grids in the ξ-direction
i	i-th spatial step in the ξ-direction
J	total number of spatial grids in the η-direction
j	j-th spatial step in the η-direction
$\mathbf{K}$	$\mu/R\rho_0 a_0$
k	bulk modulus
k_{rm}	radial wave number of the m-th radial mode

L	total length of the pipe
$\mathbf{M}$	Mach number u_0/a_0
N_r	the grid number along the pipe radius
n	n-th time step
p'	pressure
p	dimensionless pressure $(p' - p_e')/\rho_0 u_0 a_0$
p_{avg}	area-averaged pressure
p_{axis}	pressure at the pipe axis
p_{wall}	pressure at the pipe wall
p_e'	pressure at $x = 0$
R	pipe radius
r	radial coordinate from pipe centerline
Re	Reynolds number
T_{th}	system theoretical period $4L/a_0$
t	time
u_0	the initial average axial velocity
u'	axial velocity
u	dimensionless axial velocity u'/u_0

V_{gm}	group velocity of m-th radial mode
v'	radial velocity
v	dimensionless radial velocity v'/u_0
x	axial coordinate along pipe centerline
$\Delta\eta$	spatial step in the η-direction
$\Delta\xi$	spatial step in the ξ-direction
$\Delta\tau$	size of time step
η	dimensionless radial coordinate r/R
κ	volume viscosity
μ	dynamic viscosity
ξ	dimensionless axial coordinate x/R
ρ	fluid density
ρ_0	mean density of the fluid (water)
τ	dimensionless time a_0t/R
τ_0	time duration of the valve oscillation
ω	frequency in radius per second

REFERENCES

[1] Chaudhry, M. H., 2014, *Applied Hydraulic Transients*, Springer-Verlag, New York.

[2] Duan, H. F., Tung, Y. K., and Ghidaoui, M. S., 2010, "Probabilistic Analysis of Transient Design for Water Supply Systems," J. Water Resour. Plann. Manage., 136(6), pp. 678-687. DOI:10.1061/(ASCE)WR.1943-5452.0000074

[3] Wylie, E. B., Streeter, V. L., and Suo, L. S., 1993, *Fluid Transients in Systems*, Prentice-Hall, Englewood Cliffs, New Jersey.

[4] Ghidaoui, M. S., 2004, "On the Fundamental Equations of Water Hammer," Urban Water J., 1(2), pp. 71-83. DOI:10.1080/15730620412331290001

[5] Ghidaoui, M. S., Zhao, M., McInnis, D. A., and Axworthy, D. H., 2005, "A Review of Water Hammer Theory and Practice," ASME Appl. Mech. Rev., 58(1), pp. 49-76. DOI:10.1115/1.1828050

[6] Vardy, A. E., and Hwang, K. L., 1991, "A Characteristics Model of Transient Friction in Pipes," J. Hydraul. Res., 29(5), pp. 669-684. DOI:10.1080/00221689109498983

[7] Brunone, B., Ferrante, M., and Cacciamani, M., 2004, "Decay of Pressure and Energy Dissipation in Laminar Transient Flow," ASME J. Fluids Eng., 126(6), pp. 928-934. DOI:10.1115/1.1839926

[8] Zhao, M., and Ghidaoui, M. S., 2003, "Efficient Quasi-Two-Dimensional Model for Water Hammer Problems," J. Hydraul. Eng., 129(12), pp. 1007-1013. DOI:10.1061/(ASCE)0733-9429(2003)129:12(1007)

[9] Duan, H. F., Ghidaoui, M. S., and Tung, Y. K., 2009, "An Efficient Quasi-2D Simulation of Waterhammer in Complex Pipe Systems," ASME J. Fluids Eng., 131(8), p. 081105. DOI:10.1115/1.3176978

[10] Pezzinga, G., 1999, "Quasi-2D Model for Unsteady Flow in Pipe Networks," J. Hydraul. Eng., 125(7), pp. 676-685. DOI:10.1061/(ASCE)0733-9429(1999)125:7(676)

[11] Zielke, W., 1968, "Frequency-Dependent Friction in Transient Pipe Flow," ASME J. Basic Eng., 90(1), pp. 109-115. DOI:10.1115/1.3605049

[12] Martins, N. M. C., Brunone, B., Meniconi, S., Ramos, H. M., and Covas, D. I. C., 2018, "Efficient Computational Fluid Dynamics Model for Transient Laminar Flow Modeling: Pressure Wave Propagation and Velocity Profile Changes," ASME J. Fluids Eng., 140(1), p. 011102. DOI:10.1115/1.4037504

[13] Zhao, M., Ghidaoui, M. S., Louati, M., and Duan, H. F., 2018, "Numerical Study of the Blockage Length Effect on the Transient Wave in Pipe Flows," J. Hydraul. Res., pp. 1-11.. DOI:10.1080/00221686.2017.1394374

[14] Colombo, A. F., Lee, P. J., and Karney, B. W., 2009, "A Selective Literature Review of Transient-Based Leak Detection Methods," J. Hydro-environ. Res., 2(4), pp. 212-227. DOI:10.1016/j.jher.2009.02.003

[15] Lee, P. J., Duan, H. F., Ghidaoui, M. S., and Karney, B. W., 2013, "Frequency Domain Analysis of Pipe Fluid Transient Behaviour," J. Hydraul. Res., 51(6), pp. 609-622. DOI:10.1080/00221686.2013.814597

[16] Brunone, B., 1999, "Transient Test-Based Technique for Leak Detection in Outfall Pipes," J. Water Resour. Plann. Manage., 125(5), pp. 302-306. DOI:10.1061/(ASCE)0733-9496(1999)125:5(302)

[17] Brunone, B., Ferrante, M., and Meniconi, S., 2008, "Portable Pressure Wave-Maker for Leak Detection and Pipe System Characterization," J. Am. Water Works Assoc., 100(4), pp. 108-116.

[18] Covas, D., Stoianov, I., Ramos, H., Graham, N., and Maksimovic, C., 2004, "The Dynamic Effect of Pipe-Wall Viscoelasticity in Hydraulic Transients. Part I—Experimental Analysis and Creep Characterization," J. Hydraul. Res., 42(5), pp. 517-532. DOI:10.1080/00221686.2004.9641221

[19] Duan, H. F., Lee, P. J., Ghidaoui, M. S., and Tung, Y. K., 2011, "Leak Detection in Complex Series Pipelines by Using the System Frequency Response Method," J. Hydraul. Res., 49(2), pp. 213-221. DOI:10.1080/00221686.2011.553486

[20] Duan, H. F., Lee, P. J., Ghidaoui, M. S., and Tung, Y. K., 2012, "Extended Blockage Detection in Pipelines by Using the System Frequency Response Analysis," J. Water Resour. Plann. Manage., 138(1), pp. 55-62. DOI:10.1061/(ASCE)WR.1943-5452.0000145

[21] Duan, H. F., Lee, P. J., Kashima, A., Lu, J., Ghidaoui, M. S., and Tung, Y. K., 2013, "Extended Blockage Detection in Pipes Using the System Frequency Response: Analytical Analysis and Experimental Verification," J. Hydraul. Eng., 139(7), pp. 763-771. DOI:10.1061/(ASCE)HY.1943-7900.0000736

[22] Lee, P. J., Lambert, M. F., Simpson, A. R., Vítkovský, J. P., and Liggett, J. A., 2006, "Experimental Verification of the Frequency Response Method for Pipeline Leak Detection," J. Hydraul. Res., 44(5), pp. 693-707. DOI:10.1080/00221686.2006.9521718

[23] Lee, P. J., Vítkovský, J. P., Lambert, M. F., Simpson, A. R., and Liggett, J. A., 2007, "Leak Location in Pipelines Using the Impulse Response Function," J. Hydraul. Res., 45(5), pp. 643-652. DOI:10.1080/00221686.2007.9521800

[24] Liggett, J. A., and Chen, L. C., 1994, "Inverse Transient Analysis in Pipe Networks," J. Hydraul. Eng., 120(8), pp. 934-955. DOI:10.1061/(ASCE)0733-9429(1994)120:8(934)

[25] Meniconi, S., Brunone, B., Ferrante, M., Capponi, C., Carrettini, C. A., Chiesa, C., Segalini, D., and Lanfranchi, E. A., 2015, "Anomaly Pre-Localization in Distribution–Transmission Mains by Pump Trip: Preliminary Field Tests in the Milan Pipe System," J. Hydroinform., 17(3), pp. 377-389. DOI:10.2166/hydro.2014.038

[26] Meniconi, S., Duan, H. F., Lee, P. J., Brunone, B., Ghidaoui, M. S., and Ferrante, M., 2013, "Experimental Investigation of Coupled Frequency and Time-Domain Transient Test–Based Techniques for Partial Blockage Detection in Pipelines," J. Hydraul. Eng., 139(10), pp. 1033-1040. DOI:10.1061/(ASCE)HY.1943-7900.0000768

[27] Sattar, A. M., Chaudhry, M. H., and Kassem, A. A., 2008, "Partial Blockage Detection in Pipelines by Frequency Response Method," J. Hydraul. Eng., 134(1), pp. 76-89. DOI:10.1061/(ASCE)0733-9429(2008)134:1(76)

[28] Stephens, M. L., 2008, "Transient Response Analysis for Fault Detection and Pipeline Wall Condition Assessment in Field Water Transmission and Distribution Pipelines and Networks," Ph.D. thesis, Univ. of Adelaide, Adelaide, Australia.

[29] Lee, P. J., Duan, H. F., Tuck, J., and Ghidaoui, M. S., 2015, "Numerical and Experimental Study on the Effect of Signal Bandwidth on Pipe Assessment Using Fluid Transients," J. Hydraul. Eng., 141(2), p. 04014074. DOI:10.1061/(ASCE)HY.1943-7900.0000961

[30] Mitra, A. K., and Rouleau, W. T., 1985, "Radial and Axial Variations in Transient Pressure Waves Transmitted through Liquid Transmission Lines," ASME J. Fluids Eng., 107(1), pp. 105-111. DOI:10.1115/1.3242423

[31] Louati, M., and Ghidaoui, M. S., 2017, "High-Frequency Acoustic Wave Properties in a Water-Filled Pipe. Part 1: Dispersion and Multi-Path Behaviour," J. Hydraul. Res., 55(5), pp. 613-631. DOI:10.1080/00221686.2017.1354931

[32] Louati, M., and Ghidaoui, M. S., 2017, "High-Frequency Acoustic Wave Properties in a Water-Filled Pipe. Part 2: Range of Propagation," J. Hydraul. Res., 55(5), pp. 632-646. DOI:10.1080/00221686.2017.1354934

[33] Adamkowski, A., and Lewandowski, M., 2006, "Experimental Examination of Unsteady Friction Models for Transient Pipe Flow Simulation," ASME J. Fluids Eng., 128(6), pp. 1351-1363. DOI:10.1115/1.2354521

[34] Bergant, A., Simpson, A. R., and Vítkovský, J. P., 2001, "Developments in Unsteady Pipe Flow Friction Modelling," J. Hydraul. Res., 39(3), pp. 249-257. DOI:10.1080/00221680109499828

[35] Joukowsky, N. E., 1898, "'Memoirs of the Imperial Academy Society of St. Petersburg," *Proc. of the Am. Water Works Assoc.*, 24, pp. 341-424.

[36] Riasi, A., Nourbakhsh, A., and Raisee, M., 2009, "Unsteady Velocity Profiles in Laminar and Turbulent Water Hammer Flows," ASME J. Fluids Eng., 131(12), p. 121202. DOI:10.1115/1.4000557

Figure Captions List

Fig. 1 A reservoir-pipeline-valve (RPV) experimental system

Fig. 2 The initial velocity profile (solid line) and area-averaged velocity (dashed line) for laminar pipe flows

Fig. 3 Pressure time-history at the downstream valve for three different radial points

Fig. 4 Pressure time-history for various grid density at (a) the downstream valve; (b) the mid-length of the pipe

Fig. 5 Pressure time-history at (a) the downstream valve; (b) the mid-length of the pipe

Fig. 6 Cut-off frequency (dashed line) and group velocity for each mode

Fig. 7 The temporal variations of pressure at the downstream valve

Fig. 8 (a) Radial pressure profiles at nine time points within one period of the pressure fluctuation; (b) the pressure signal after valve closure in the frequency domain

Fig. 9 The temporal variations of pressure at mid-length of the pipe

Fig. 10 The change of velocity profile (before and after the wave front) at mid-length of the pipe

Fig. 11 The temporal variations of pressure at the downstream valve

Fig. 12 (a) Radial pressure profiles at nine time points within one period of the

valve oscillation; (b) the pressure signal during the valve oscillation in the frequency domain

Fig. 13 (a) Radial pressure profiles at nine time points within one period of the the pressure fluctuation after the valve closure; (b) the pressure signal after the valve closure in the frequency domain

Fig. 14 The temporal variations of pressure at mid-length of the pipe

Fig. 15 The temporal variations of pressure at the downstream valve

Fig. 16 (a) Radial pressure profiles at nine time points within one period of the valve oscillation; (b) the pressure signal during the valve oscillation in the frequency domain

Fig. 17 (a) Radial pressure profiles at nine time points within one period of the the pressure fluctuation after valve closure; (b) the pressure signal after the valve closure in the frequency domain

Fig. 18 The temporal variations of pressure at mid-length of the pipe

Table Caption List

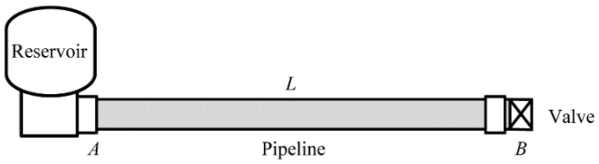

Fig. 1 A reservoir-pipeline-valve (RPV) experimental system

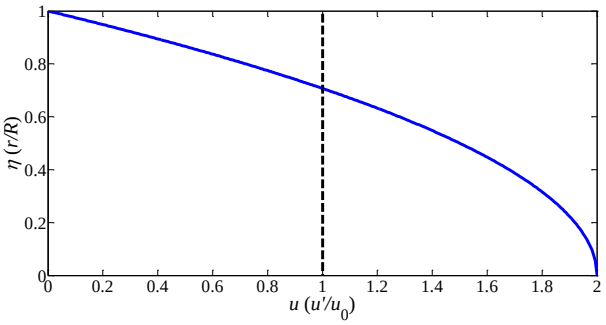

Fig. 2 The initial velocity profile (solid line) and area-averaged velocity (dashed line) for laminar pipe flows

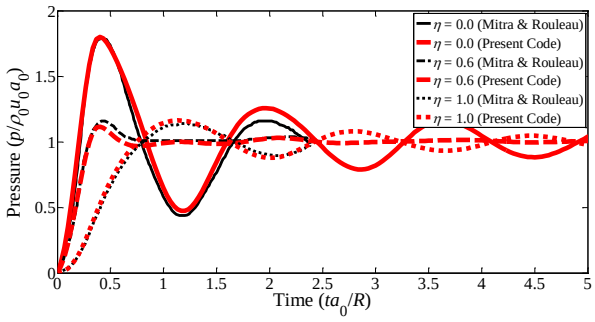

Fig. 3 Pressure time-history at the downstream valve for three different radial points

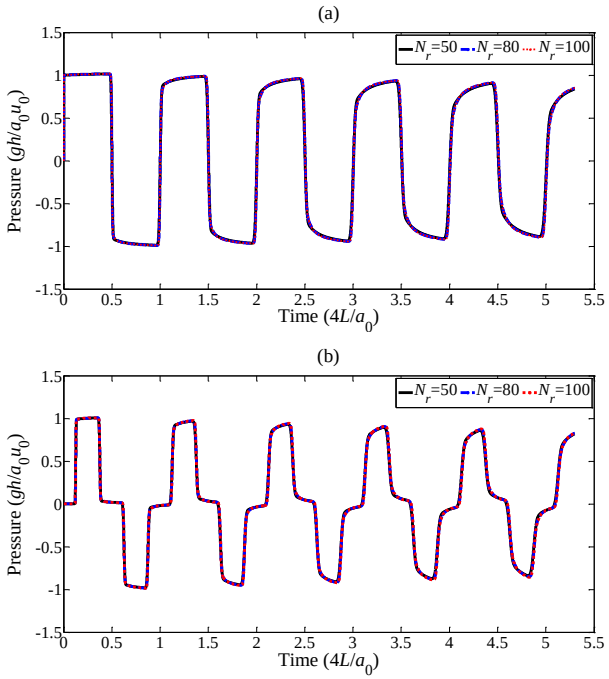

Fig. 4 Pressure time-history for various grid density at (a) the downstream valve; (b) the mid-length of the pipe

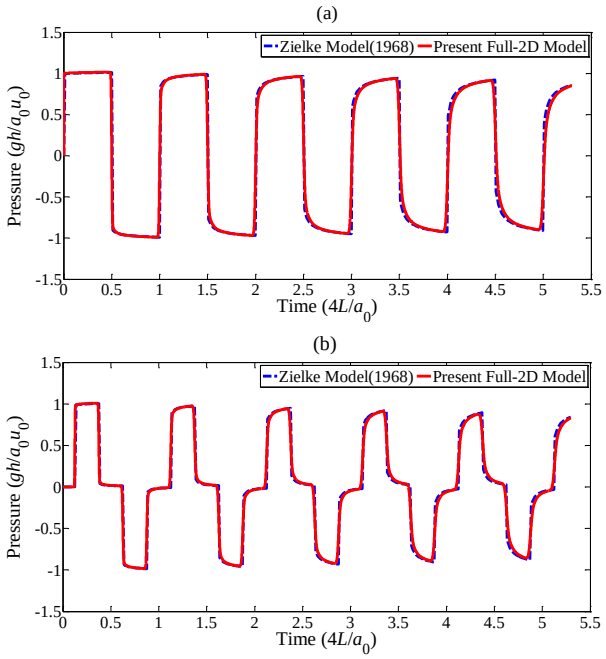

Fig. 5 Pressure time-history at (a) the downstream valve; (b) the mid-length of the pipe

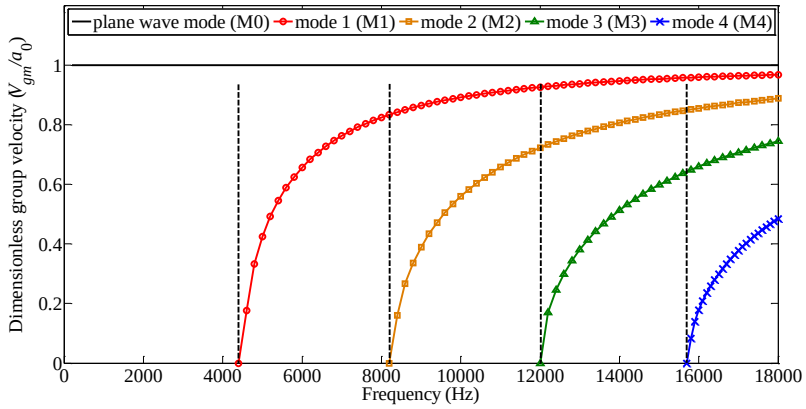

Fig. 6 Cut-off frequency (dashed line) and group velocity for each mode

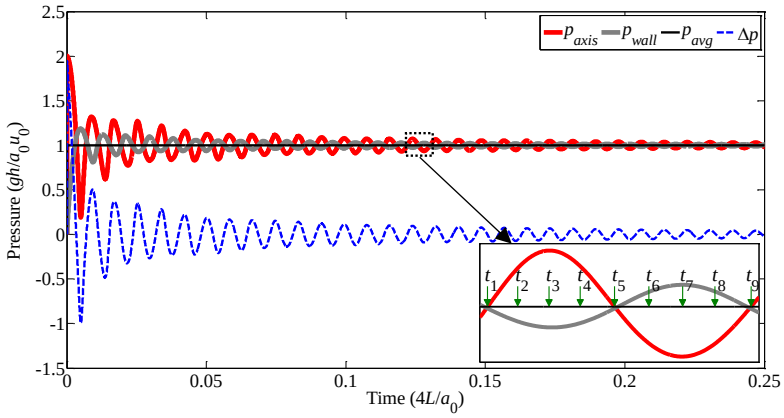

Fig. 7 The temporal variations of pressure at the downstream valve

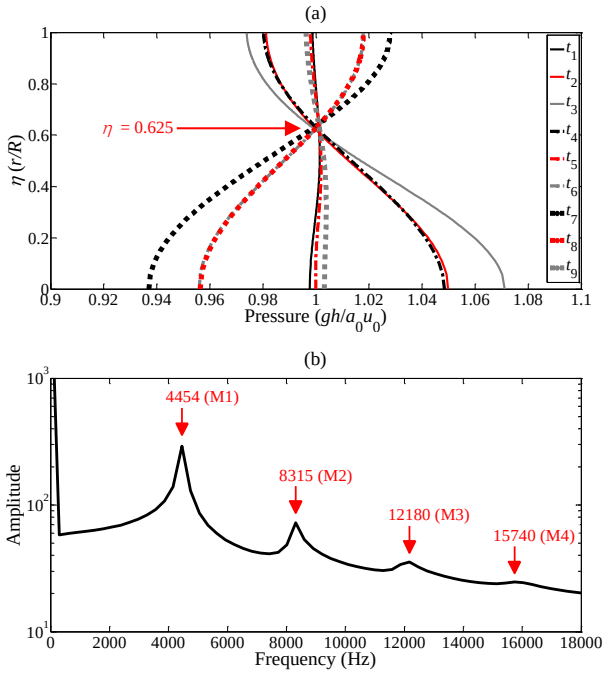

Fig. 8 (a) Radial pressure profiles at nine time points within one period of the pressure fluctuation; **(b)** the pressure signal after valve closure in the frequency domain

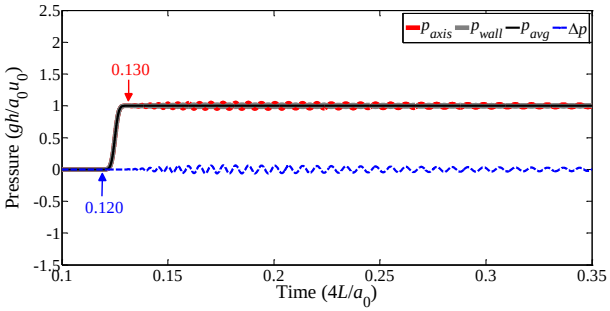

Fig. 9 The temporal variations of pressure at mid-length of the pipe

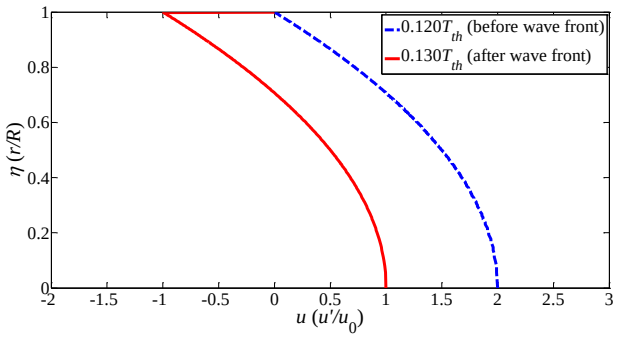

Fig. 10 The change of velocity profile (before and after the wave front) at mid-length of the pipe

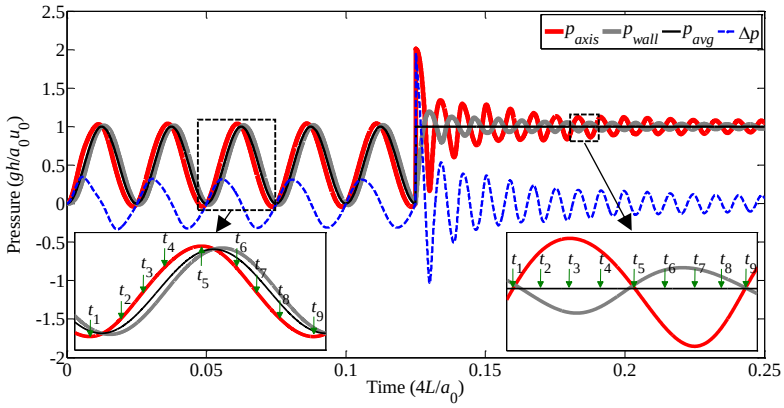

Fig. 11 The temporal variations of pressure at the downstream valve

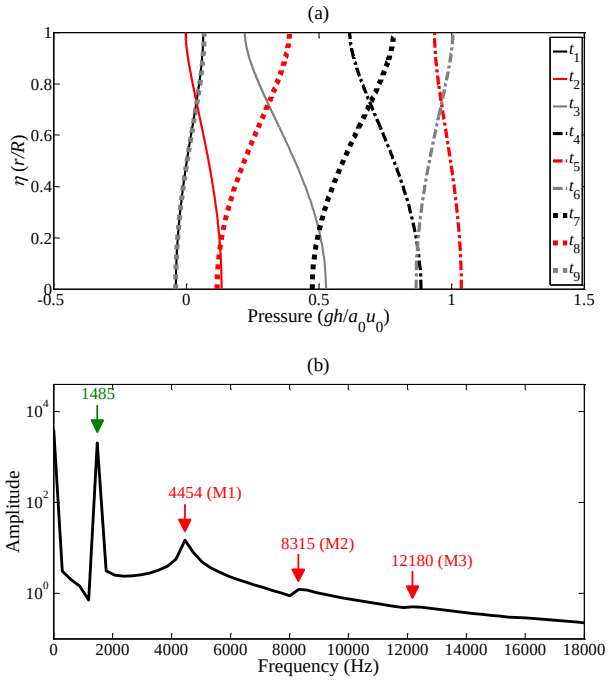

Fig. 12 (a) Radial pressure profiles at nine time points within one period of the valve oscillation; **(b)** the pressure signal during the valve oscillation in the frequency domain

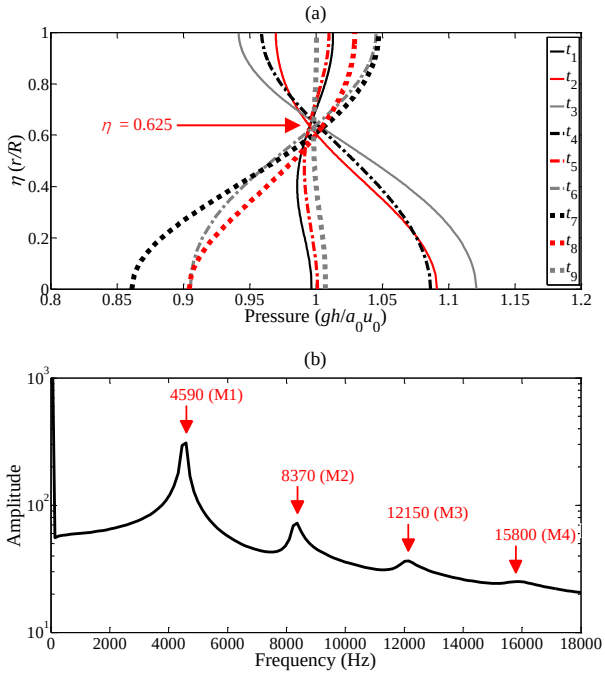

Fig. 13 (a) Radial pressure profiles at nine time points within one period of the the pressure fluctuation after the valve closure; **(b)** the pressure signal after the valve closure in the frequency domain

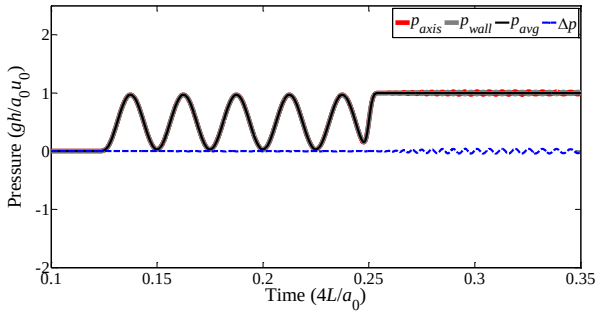

Fig. 14 The temporal variations of pressure at mid-length of the pipe

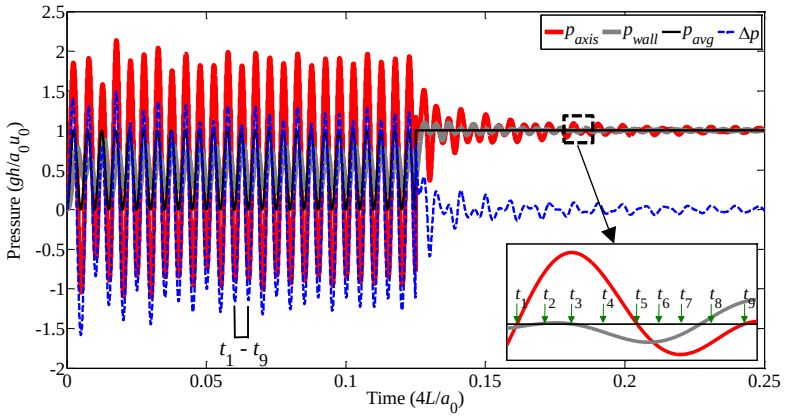

Fig. 15 The temporal variations of pressure at the downstream valve

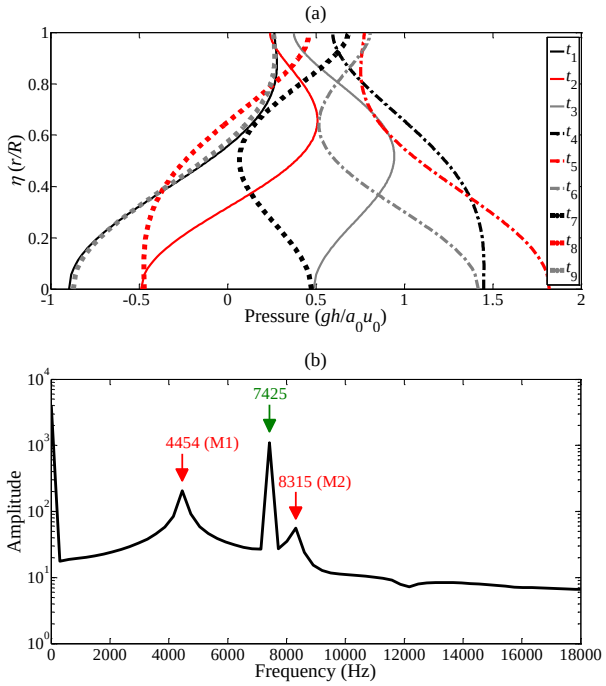

Fig. 16 (a) Radial pressure profiles at nine time points within one period of the valve oscillation; **(b)** the pressure signal during the valve oscillation in the frequency domain

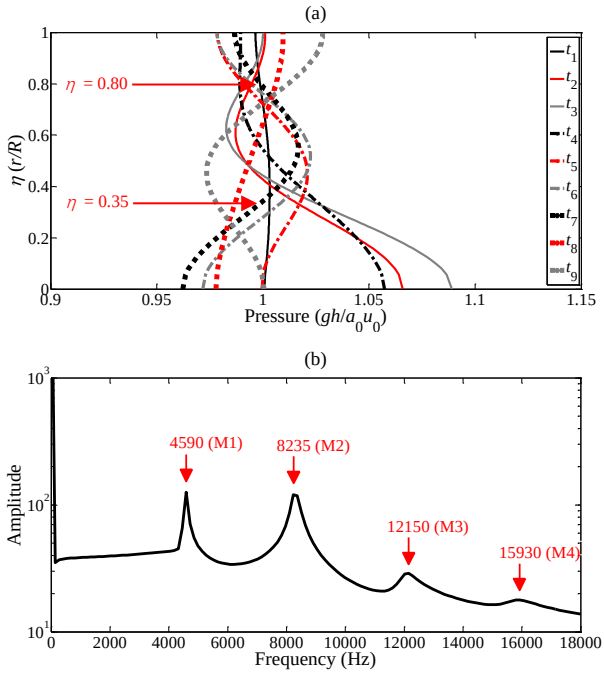

Fig. 17 (a) Radial pressure profiles at nine time points within one period of the the pressure fluctuation after valve closure; **(b)** the pressure signal after the valve closure in the frequency domain

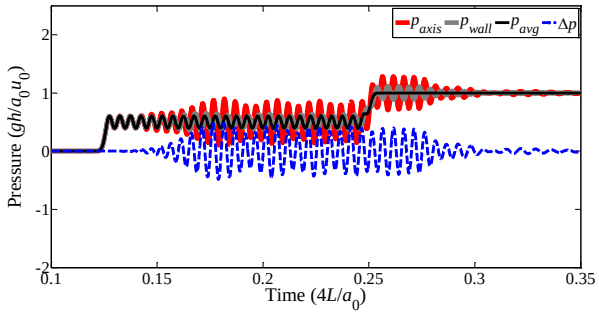

Fig. 18 The temporal variations of pressure at mid-length of the pipe

Table 1 System parameters of the numerical experiment conducted by Mitra and Rouleau [30]

a_0 (m/s)	R (m)	μ/ρ_0 (m^2/s)	Re	τ_0	$\Delta\tau = \Delta\xi = \Delta\eta$
1325	1.25e-02	3.97e-05	100	0.4	0.05

Table 2 System parameters of numerical experiments for grid independent tests (Re = 100)

a_0 (m/s)	R (m)	L (m)	μ/ρ_0 (m^2/s)	τ_0	N_r
1325	0.2	10	3.97e-05	0	50
1325	0.2	10	3.97e-05	0	80
1325	0.2	10	3.97e-05	0	100

Table 3 System parameters of three numerical applications ($\mathrm{Re} = 100$)

Test No.	L/R	a_0 (m/s)	μ/ρ_0 (m^2/s)	τ_0	Valve operation
1	50	1485	1e-6	0	Sudden closure
2	50	1485	1e-6	$0.125T_{th}$	oscillation $f_{in1} = 0.2f_r$
3	50	1485	1e-6	$0.125T_{th}$	oscillation $f_{in2} = 1.0f_r$